Chemical Science

Accepted Manuscript

This article can be cited before page numbers have been issued, to do this please use: G. Feng, Y. Fan, L. Diao, Z. Miao and J. Zhou, *Chem. Sci.*, 2026, DOI: 10.1039/D5SC06257H.

ROYAL SOCIETY OF CHEMISTRY

rsc.li/chemical-science

View Article Online
DOI: 10.1039/D5SC06257H

Pd-Cu Dual Sites Turning H Adsorption for Efficient Electrocatalytic Hydrogenation of HMF

Authors:

Guozhou Feng[a] Yuxin Fan[a] Lechen Diao[a*] Zhichao Miao[a] and Jin Zhou[a*]

Affiliations:

a School of Chemistry and Chemical Engineering, Shandong University of Technology, Zibo 255000, PR China

* Corresponding author

View Article Online
DOI: 10.1039/D5SC06257H

Pd-Cu Dual Sites Turning H Adsorption for Efficient Electrocatalytic Hydrogenation of HMF

View Article Online
DOI: 10.1039/D5SC06257H

Abstract

Electrocatalytic hydrogenation (ECH) of 5-hydroxymethylfurfural (HMF) to 2,5-bis(hydroxymethyl)furan (BHMF) is regarded as a green synthesis strategy for generating high quality bio-based chemicals. However, simultaneously regulating both the hydrogen (H) coverage and the adsorption behavior of HMF presents a significant challenge, particularly in unraveling the intricate structure–activity relationship and achieving a selective target product. Here, we enhance the availability of hydrogen (H*) and modulate surface electronic interactions with 5-hydroxymethylfurfural (HMF) to facilitate selective electrochemical hydrogenation (ECH) of HMF by introducing palladium as an auxiliary component. Pd-Cu dual sites synergistically enhanced H* supplement and HMF activation while suppressing competing hydrogen evolution reaction. The optimized electrocatalyst exhibits notable catalytic performance, attaining a selectivity of 99.3% and a Faradaic efficiency for BHMF of 97.5% at a potential of −1.15 V (vs Ag/AgCl). Density functional theory (DFT) calculations demonstrate that the Pd doping is crucial for enhancing the adsorption of H* and HMF* intermediates, thereby promoting the hydrogenation of HMF along with the Langmuir-Hinshelwood (L-H) mechanism under neutral conditions. This work establishes a catalyst design paradigm where atomic-level dopant engineering regulates multistep protonation kinetics, offering fundamental insights into biomass electrorefining.

Keyword: biomass upgrading; electrocatalytic hydrogenation reaction; 5-hydroxymethylfurfural; 2,5-bis(hydroxymethyl)furan; dual sites turning

View Article Online
DOI: 10.1039/D5SC06257H

Introduction

With the depletion of traditional fossil resources and increasing demand for fine chemicals and polyester materials, the conversion of biomass into platform chemicals is getting increasing attention due to their relevance in sustainable development. Featuring both hydroxyl and aldehyde functional groups, HMF serves as a versatile precursor that can be transformed into high-value derivatives through selective chemical modifications.[1-7] The directional catalytic reduction the aldehyde group of HMF to yield 2,5-bis(hydroxymethyl)furan (BHMF), a dihydroxy-containing compound which serves as a key precursor for pharmaceutical intermediates and advanced polymer materials.[8, 9] Current industrial processes predominantly employ conventional thermal catalysis for HMF hydrogenation under the high-pressure H_2 and elevated temperatures conditions, during which accompanied with excessive hydrogenolysis and hydrogenation of furan ring.[10, 11] This has driven research interest in developing alternative hydrogenation methods that operate under milder conditions without gaseous H_2. Electrochemical hydrogenation is considered a promising approach, utilizing H from H_2O under ambient conditions, thereby eliminating the need for external H_2 supply.[12, 13] This green eco-friendly synthesis strategy enables selective production of BHMF through direct electron transfer processes, aligning with sustainable energy utilization principles.[14] What's more, electrocatalytic hydrogenation reaction can achieve better target product selectivity by controlling the catalyst and potential.[15]

View Article Online
DOI: 10.1039/D5SC06257H

The prevailing mechanism for electrochemical hydrogenation of HMF is L-H mechanism, through water splitting to produce H adsorbed on the electrode surface (denoted as H*), followed by H* reacts with HMF* to produce BHMF.[16-18] Mostly, Cu-based catalysts exhibit inferior activity for electrocatalytic hydrogen evolution reaction (HER) while exhibiting superior selectivity for hydrogenation due to its abundantly d-orbital electrons, which regarded as potential catalysts for the efficient electrosynthesis of BHMF.[19, 20] Nevertheless, studies find that pure Cu species struggle to balance the HMF activation and H* supply capability simultaneously. As a result, the intermediate products (HMF*) generated from electrochemical adsorption are not hydrogenated promptly, leading to HMF dimerization. To address this challenge, researchers have developed various Cu-based catalysts, including Ga-doped Ag-Cu[21], PMo_{12}/Cu[22], RhCu[23], Cu/MOx Cu[24], and CuFeOx/CF[25], all demonstrating enhanced HMF hydrogenation performance in aqueous media under mild conditions. These designs primarily aim to optimize the balance between HMF adsorption and H* availability through synergistic effects from secondary components. While increased H* surface coverage proves critical for efficient hydrogenation, a paradoxical competition emerges: excessive H* tends to recombine into H_2 gas, significantly reducing the Faradaic efficiency toward BHMF production.[21] This fundamental trade-off highlights the necessity for precision engineering of catalysts. Therefore, introducing suitable proton supplying sites might provide H* with appropriate protonation capability, which facilitates efficient and selective hydrogenation of HMF to BHMF.

Pd is a group VIII element known for its strong O-H activation and proton affinity.

View Article Online
DOI: 10.1039/D5SC06257H

Among transition metals, it locates at the top and center-left of the hydrogen evolution reaction (HER) volcano plot highlights its potential as an ideal element to generate sufficient *H without causing excessive HER. In addition, Pd-based materials were usually used to activate HMF.[26, 27] Therefore, introducing Pd atoms into Cu-based catalysts may balance H* supply ability and HMF adsorption behavior of catalysts, significantly improve its electrocatalytic HMF hydrogenation performance.

Herein, we report a rationally designed Pd-Cu heterostructure catalyst supported on three-dimensional carbon matrices (denoted as x%Pd-Cu@3DC, where x indicates Pd molar fractions) for electrochemical upgrading of HMF to BHMF. The optimized 3%Pd-Cu@3DC electrocatalyst demonstrates exceptional performance metrics at an applied potential of −1.45 V (versus Ag/AgCl), achieving 97% HMF conversion efficiency, 99.3% BHMF selectivity, and 97.5% Faradaic efficiency, substantially outperforming monometallic Cu catalysts and other Cu-based catalysts. Mechanistic analysis reveals two interdependent functions facilitated by atomic-level Pd incorporation. On one hand, Pd sites synergistically promote water splitting to generate reactive hydrogen species (H*), enabling rapid hydrogenation of the critical $C_6H_7O_3$* intermediate. On the other hand, the interaction between Cu and Pd atoms could also modulate the electronic structure of the catalyst, which enhances the absorption of HMF and the selectivity protonation of *CHO.[28] This catalyst design strategy certifies that suitable proton-supplying sites can effectively regulate the multiple protonation steps to facilitate the HMF to BHMF.

View Article Online
DOI: 10.1039/D5SC06257H

Results and discussion

Catalysts Synthesis and Characterization.

The Pd-Cu@3DC catalysts were fabricated through a modified lyophilization-calcination synthesis strategy (**Figure 1a**)[29]. Initially, a homogeneous precursor solution was prepared by dissolving $PdCl_2$, $Cu(NO_3)_2$, glucose, and NaCl in deionized water. This solution subsequently underwent freeze-drying at -20 ˚C for 20 h, followed by thermal annealing at 700 ˚C for 2 h under H_2/Ar atmosphere. The resulting carbonaceous composite was then subjected to thorough aqueous washing to eliminate NaCl templates, ultimately yielding hierarchically porous honeycomb architectures with atomic-level Pd-Cu coordination nanoparticles.

Microstructural characterization reveals critical morphological features of the Pd-Cu@3DC catalyst. Scanning electron microscopy (SEM) and transmission electron microscopy (TEM) analyses (**Figure S1**, **Figure 1b**) demonstrate the formation of three-dimensionally interconnected ultrathin carbon skeletons with hierarchical porosity, establishing continuous conductive pathways for efficient electron transfer and electrolyte infiltration. Through the Spherical Aberration Corrected Transmission Electron Microscope (AC-STEM) in **Figure 1c**, distinct isolated bright spots were identified. We measured the interplanar spacing and found that it increased by 0.02 nm compared with that of the (200) plane in the standard Cu reference card (0.181 nm). The presence of a single Pd atom within a column of Cu atoms indicates that the Pd atom exists in a single-atom form. Energy-dispersive spectroscopy (EDS) mapping

View Article Online
DOI: 10.1039/D5SC06257H

images (Figure 1d) showed the distribution contours of Cu and Pd elements highly overlapped with the STEM images，suggesting partial substitution of Cu atoms by Pd. Crystallographic analysis of the Pd-Cu@3DC catalysts was performed through X-ray diffraction (XRD) patterns. The XRD patterns (**Figure S2a**) display characteristic diffraction peaks at 43.3°, 50.4°, 74.1°, and 89.9°, indexed to the (111), (200), (220), and (311) planes of face-centered cubic (fcc) Cu (JCPDS 04-0836). Additional reflections at 35°, 36.4°, 37°, and 62° in well agreement with the peaks of monoclinic CuO (JCPDS 44-0706), and the peak at 36.4° correspond to Cu_2O (JCPDS 05-0667), which arising from surface oxidation during ambient exposure. Notably, substituting smaller ions with larger counterparts induces lattice expansion, which in turn increases the interplanar spacing *d*. As dictated by Bragg's law ($n\lambda = 2d\sin\theta$), with a fixed X-ray wavelength (λ), an increase in *d* inevitably leads to a decrease in sinθ. This phenomenon c

onsequently results in a shift of the diffraction angle (θ) toward lower values. All Cu-related peaks exhibit a systematic negative shift of 0.15–0.23° compared to pristine Cu@3DC (**Figure 1e**), indicative of lattice expansion caused by partial substitution of smaller Cu atoms (r = 0.128 nm) with larger Pd atoms (r = 0.137 nm). This, together with the AC-STEM results, indicates that Pd is incorporated into the catalyst as single atoms. **Figure S2b** shows the Raman spectra of the 3%Pd-Cu@3DC, where three prominent peaks show at 1350 and 1580 cm^{-1}, corresponding to the D peak (amorphous carbon) and G peak (crystalline graphite), respectively. The peaks intensity ratios value (I_D/I_G) of the 3%Pd-Cu@3DC are about 0.14, reflecting that the high graphitization

View Article Online
DOI: 10.1039/D5SC06257H

degrees of the samples due to the catalysis role of Cu. As shown in Figure S13, the XRD patterns of 3% Pd-Cu@3DC before and after reduction reveal that the characteristic diffraction peaks corresponding to CuO and Cu_2O have vanished. Given that the catalyst was supported on carbon paper for XRD measurements, several extra characteristic diffraction peaks of carbon paper are detected in comparison with other XRD patterns.

X-ray photoelectron spectroscopy (XPS) characterization was performed to recognize the chemical valence types of the Pd-Cu@3DC catalysts. As exhibited in **Figure 1f-1g**, the characteristic peaks of Cu 2p and Pd 3d are located at the same position in the four samples. The Cu 2p high-resolution XPS spectra can be divided into four subpeaks, representing Cu^0/Cu^+ species ($2p_{3/2}$, 933.8 eV; $2p_{1/2}$, 954.4 eV) and Cu^{2+} species ($2p_{3/2}$, 935.7 eV; $2p_{1/2}$, 955.8 eV), respectively. Notably, Cu atoms show a slight surface oxidation in the Pd-Cu@3DC. With the increasing Pd doping, the valence state of Cu atoms transforming from +2 valence to +1/0 valence. Moreover, the Pd 3d XPS spectra of the Pd-Cu@3DC exhibits an obvious oxidized state compared to monometallic Pd@3DC. These results indicate the successful incorporation of Pd into the Cu nanoparticles and electrons transformation from Pd to Cu within the alloy structure.

View Article Online
DOI: 10.1039/D5SC06257H

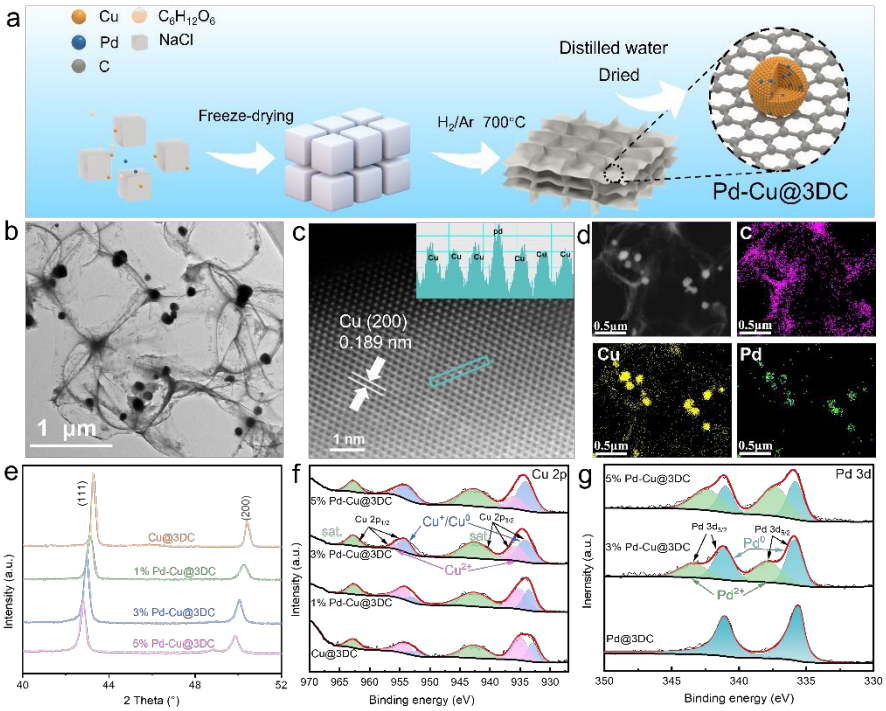

Figure 1. Synthetic routes and structural characterization for Pd-Cu@3DC. (a) Illustration of the synthetic routes. (b) TEM image, (c) AC-STEM image. (d) EDS mapping images of 3%Pd-Cu@3DC. (e) XRD patterns of 3%Pd-Cu@3DC. High-resolution XPS spectra of (f) Cu 2p and (g) Pd 3d of 3%Pd-Cu@3DC.

Electrocatalytic Hydrogeneration Performance

Before assessing the catalytic performance of the Pd-Cu@3DC towards HMF hydrogenation, the CuO and Cu_2O on the surface of pd-Cu nanoparticles were first reduced into metal by galvanostatic test. Then, the linear sweep voltammetry (LSV) curves were examined in 0.5 M $KHCO_3$ solution (pH~8.17) with or without adding 50 mM HMF. As shown in **Figure 2a-b**, incorporation of the Pd atom into Cu significantly reduces the overpotential of the HER. Moreover, the presence of HMF further decreases the overpotential of the reaction process, which indicates that Pd-Cu@3DC is active in

View Article Online
DOI: 10.1039/D5SC06257H

electrocatalysis the HMF hydrogenation. The catalytic kinetics curves of the catalyst for HER and HMF hydrogenation are shown in **Figure 2c** through the Tafel plots derived from polarization curves.[30] The Tafel slopes of Cu@3DC and 3%Pd-Cu@3DC for HER were 271.99 and 504.52 mV dec^{-1}, respectively, illustrating that the Volmer step dominates the HER rate.[31] Meanwhile, as demonstrated by the attenuated total reflection surface-enhanced infrared absorption spectroscopy (ATR-SEIRAS) spectra in **Figure S12a-b**, the complete absence of the adsorbed hydroxyl (OH*) stretching band at 3256 cm^{-1} provides definitive evidence that H* is generated via the Volmer step ($H_2O + e^- \rightarrow H^* + OH^-$), with the generated OH^- transferring to the electrolyte solution.[32] For the HMF hydrogenation reaction, the Tafel slopes Cu@3DC and 3%Pd-Cu@3DC were measured to be 302.05 and 132.97 mV dec^{-1}, respectively. Both values are lower compared to those obtained by HER. These results suggest that the HMF hydrogenation process holds greater advantage over the HER process.

The electrocatalytic hydrogenation performance was systematically evaluated through chronoamperometric analyses in 50 mM HMF electrolyte, with reaction products quantified via HPLC (**Figure 2d**, **Figure S3**). **Figure 2e** and **Figure S4** compares the potential-dependent activity profiles of Cu@3DC and Pd-Cu@3DC catalysts. The monometallic Cu@3DC exhibits limited conversion efficiency (<25%) and Faradaic efficiency (FE<30%) across the tested potential window (-1.1 to -1.3 V vs Ag/AgCl), despite maintaining 95-98% BHMF selectivity. The 3%Pd-Cu@3DC catalyst demonstrates superior catalytic performance. As the potential increased, the efficiency of H* generation improved. As a result, the catalytic performance gradually

View Article Online
DOI: 10.1039/D5SC06257H

improved. When the potential reached at -1.15 V (vs Ag/AgCl), 3%Pd-Cu@3DC achieves near-completely (97%) conversion efficiency, 97.5% FE, and 99.3% BHMF selectivity, outperforming the Cu@3DC under identical conditions. Further increases in the potential lead to a decline in HMF conversion and FE due to intense competition for HER. A multivariate radar chart (**Figure 2f**, **Figure S4**) highlights the tripartite performance superiority (conversion, selectivity, FE) of 3%Pd-Cu@3DC over other Pd-Cu@3DC catalysts, establishing its optimal catalytic functionality. To gain deeper insights into the origin of the electrode performance for HMF hydrogenation, the electrochemical active surface area (ECSA) was evaluated based on the double-layer capacitance (C_{dl}) at different scan rates (**Figure S11**). Compared with Cu@3DC (2.4 mF cm^{-2}), the C_{dl} of 3% Pd-Cu@3DC (13.2 mF cm^{-2}) is significantly increased, exhibiting more accessible active sites for HMF adsorption. To accurately evaluate the intrinsic catalytic capability of the synthesized materials, the electrochemical performance was normalized by the ECSA, considering that the apparent activity could be affected by the difference in ECSA. As shown in **Figure S11d**, the normalized current density of 3% Pd-Cu@3DC reaches -0.0042 mA cm_{ECSA}^{-2} at -1.15 V (vs. Ag/AgCl), which is 1.5 times that of Cu@3DC, indicating the enhanced intrinsic catalytic activity induced by Pd doping.

In addition to the potentials, the influence of concentrations on conversion and FE were also evaluated in **Figure 2g**. Concentration-dependent studies reveal a positive correlation between HMF concentration (20-50 mM) and ECH efficiency for 3%Pd-Cu@3DC, with maximum values reaching 97% conversion and 97.5% FE at 50 mM

View Article Online
DOI: 10.1039/D5SC06257H

HMF. This enhancement stems from suppressed hydrogen evolution reaction (HER) kinetics at elevated substrate concentrations, where competitive HMF adsorption dominates active sites. Notably, 3%Pd-Cu@3DC maintains exceptional operational stability, preserving 99.1% BHMF selectivity even at 100 mM HMF, though with moderate efficiency declines (conversion: 94.2%, FE: 92.5%). These reductions arise from mass transport limitations and insufficient H* under high substrate concentrations. Interestingly, bis(hydroxymethyl)hydrofuroin (BHH) was not observed throughout the entire reaction process, which is different from previous reports. According to previous report, if catalyst interacts with the HMF as the oxygen coordination configuration, it prefers to promote the two-electron production of -CH_2OH via an R–CH_2–O* intermediate.[33, 34]

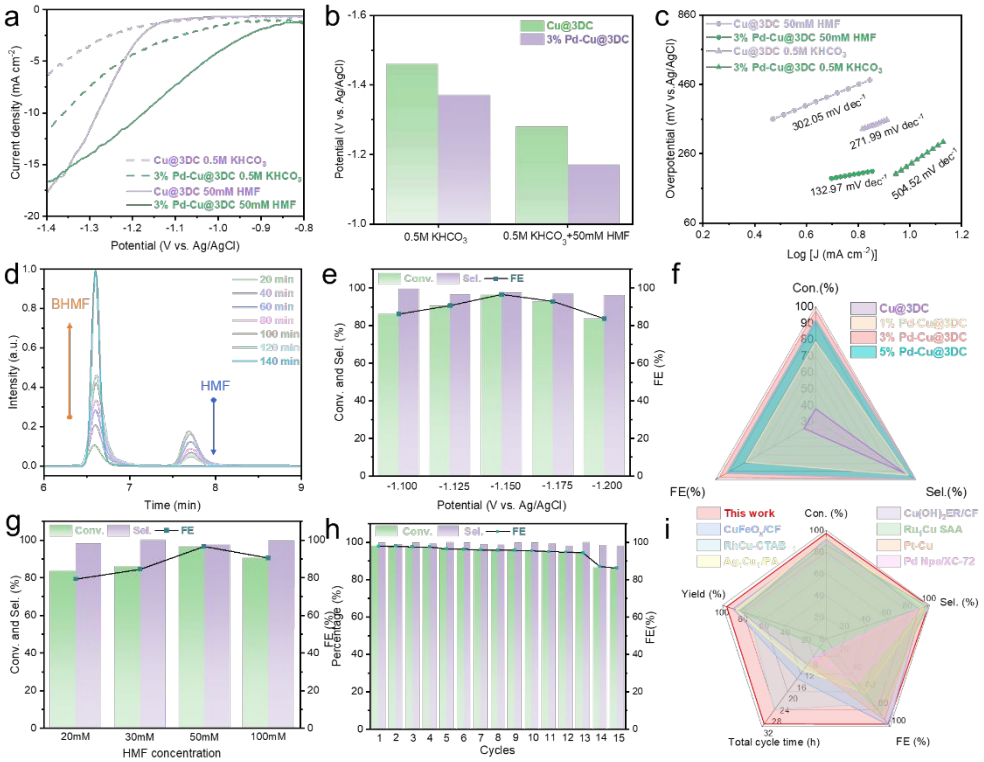

Figure 2. Electrochemical performance of the catalysts. (a) LSV curves (b) potential

View Article Online
DOI: 10.1039/D5SC06257H

comparison (at 10 mA cm^{-2}) and (c) Tafel slope of Cu@3DC and 3% Pd-Cu@3DC in 0.5 M $KHCO_3$ solution with and without 50 mM HMF. (d) HPLC curves of the electrolyte at different electrolysis times. (e) Potential screening of chronoamperometric electrolysis HMF on 3%Pd-Cu@3DC. (f) Performance comparison of different Pd-Cu@3DC. (g) Catalysis performance of 3%Pd-Cu@3DC at different HMF concentrations. (h) Cyclic electrolysis stability of 3%Pd-Cu@3DC. (i) Performance comparison with literature (The data comes from **Table S1**).

Long-term stability is critical for electrocatalysts intended for industrial applications. Consecutive chronoamperometric electrolysis was performed to evaluate the stability of the 3%Pd-Cu@3DC catalyst. As shown in **Figure 2h**, the 3%Pd-Cu@3DC catalyst displays robust performance throughout 13 successive electrolysis experiments. The HMF conversion and FE remain consistently above 95% during all cycles, suggesting its excellent stability of 3%Pd-Cu@3DC. In comparison with analogous reports in the literature, the 3%Pd-Cu@3DC catalyst exhibits outstanding hydrogenation performance for HMF (**Figure 2i**, **Table S1**).

Reaction Kinetics Analysis

Kinetic experiments were conducted to get insights into the reaction process for the electrochemical hydrogenation of HMF over Cu@3DC and 3%Pd-Cu@3DC. We tracked the concentration, selectivity, and FE of BHMF during HMF electrochemical hydrogenation. As presented in **Figure 3a**, HMF was gradually consumed in the electrolyte, while the BHMF quickly increased with the reaction proceeding.

View Article Online
DOI: 10.1039/D5SC06257H

Correspondingly, selectivity and FE maintain up to 95% during the electroreduction process. On account of the these experimental results, a simplified reaction model was developed to investigate the kinetics for the electrochemical hydrogenation of HMF over Cu@3DC and 3%Pd-Cu@3DC (**Figure 3b**, **Figure S5**)[35]. The kinetic behavior was hypothesized to be the pseudo first order reaction for this reaction step in which the H_2O concentration was constant, and the kinetic equation can be seen in **Figure 3b**. Notably, after the introduction of Pd atoms, the reaction rate constants (k) of 3%Pd-Cu@3DC significantly increased compared with that of Cu@3DC, indicating that the Pd dopant could promote the electrochemical hydrogenation reaction. To better comprehend catalytic reactions, it is crucial to determine the apparent activation energy (Ea). Then, Arrhenius plots originated from k estimated at three different temperatures (20 ~ 60 ˚C) were shown in **Figure 3c** and **Figure S6c**. All curves were fitted with a correlation coefficient above 0.99, suggesting well linearly correlation.[36] Ea were obtained from the slope of the Arrhenius plots, while the pre-exponential frequency factor was corresponding to the intercept. Obviously, the Ea for Cu@3DC is 2.1 kJ mol^{-1}, while the Ea of 3%Pd-Cu@3DC significantly decreased down to 1.45 kJ mol^{-1}. The lower energy barrier is beneficial for accelerating reaction.

Charge transfer kinetics at the electrode interface is crucial role in electrocatalytic reaction. The Nyquist and Bode plots were further examined through operando electrochemical impedance spectroscopy (EIS) within the potential window of 1.0 ～ 1.3 V. As displayed in **Figure 3d**, the semicircle of 3%Pd-Cu@3DC catalyzed HMF electrochemical hydrogenation are notably smaller than those of blank group without

View Article Online
DOI: 10.1039/D5SC06257H

HMF under the same operating condition, indicating that the HMF addition has reduced the resistance at the reaction interface. This trend is more apparent for 3%Pd-Cu@3DC than Cu@3DC in **Figure S6a**. Ulteriorly, the charge transfer behaviors were investigated in the Bode plots (**Figure 3e-f**). The peak of the blank group at low frequency region corresponds to the Volmer step. Owing to the slow kinetics of Tafel step and Heyrovsky step under the low potentials, the H* on the surface of catalyst is hard to generate H_2 and the Volmer step is easy to achieve dynamic equilibrium, which leads to no electron transfer occurring on reaction interface. After introducing the HMF, the peak intensity weakens obviously and peak position shifts to higher frequency, attributing to the consuming of H* by the aldehyde groups in the HMF, which breaks the dynamic equilibrium of Volmer step and the HMF hydrogenation step predominate the next reaction.[37] When the potential increases to 1.2V, the peaks of both blank and experimental groups shift to higher frequency, showing a less difference between the two peaks. This is attributed to the HER predominates the main reaction at the high operation potential.

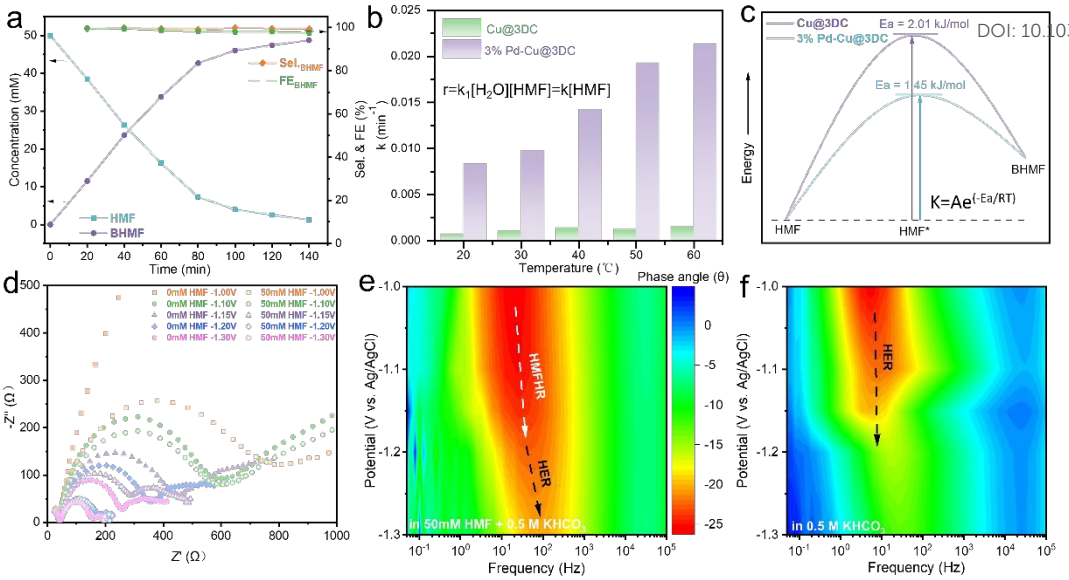

Figure 3. Reaction kinetic analysis of the ECH. (a) HPLC quantitative results at -1.15 V vs. Ag/AgCl on 3%Pd-Cu@3DC. (b) Reaction rate constant k at reaction temperature from 20~60˚C on 3%Pd-Cu@3DC and Cu@3DC. (c) Ea of electrochemical HMF hydrogenation on 3%Pd-Cu@3DC and Cu@3DC. (d-f) EIS characterization of 3%Pd-Cu@3DC, (d) Nyquist and (e-f) Bode plots.

Electrocatalytic Reaction Mechanism

As the H* availability plays a vital role in determining the kinetics of HMF hydrogenation, especially for its selectivity and FE. Cyclic voltammograms (CV) tests were carried out in $KHCO_3$ electrolyte to investigate the H* coverage on catalysts surface. As shown in **Figure 4a**, the curves show a pair redox peaks in the anodic scan for 3%Pd-Cu@3DC, which correspond to H* adsorption and desorption.[38] The 3%Pd-Cu@3DC possesses an apparent H* desorption peak, indicating exist large H* on the surface of electrode, which will lead to additional HER reactions and lower FE. After the addition of HMF, the desorption peaks of H* became smaller and were completely

View Article Online
DOI: 10.1039/D5SC06257H

suppressed in both samples at 20 mM HMF. Meanwhile, the adsorption peaks shift towards positive potential, implying HMF adsorption occurred prior to H* adsorption, which may occupy the sites of H*. Thus, the decreased H* adsorption can be attribute to the consumption by HMF reduction and the HMF adsorption.[39]

The local pH evolution during HMF electrochemical hydrogenation was quantitatively monitored using a rotating ring-disk electrode (RRDE) system through ring open-circuit potential (OCP) measurements (**Figure 4b**).[40, 41] A calibration curve was first established by correlating OCP (vs Ag/AgCl) with bulk electrolyte pH, which coincides with the Nernst equation in reply to the change of pH (**Figure S7**). RRDE analysis revealed significant interfacial pH variations of 3%Pd-Cu@3DC and Cu@3DC catalysts. For 3%Pd-Cu@3DC, the electrode-electrolyte interface pH increased from 8.9 to 9.4 as the applied potential shifted from -1.1 V to -1.2 V vs Ag/AgCl, indicative of rapid formation of reactive hydrogen species (H*) and OH^- through splitting H_2O. In contrast, the pH values of the Cu@3DC surface are much lower than those of 3%Pd-Cu@3DC, reflecting sluggish OH^- production. This pH gradient difference provides direct mechanistic evidence for the enhanced H* availability on Pd-Cu@3DC, where atomic Pd sites facilitate water dissociation ($H_2O+e^- \rightarrow H^* + OH^-$) (**Figure 4c**). The synergistic effect creates a self-sustaining alkaline microenvironment that accelerates HMF → BHMF conversion kinetics while suppressing competitive H_2 evolution through localized OH^- accumulation.

In order to further validate the supposition, tert-butyl alcohol (t-BuOH) was used

View Article Online
DOI: 10.1039/D5SC06257H

to scavenge the H* species.[42] As shown in **Figure 4d**, a notably decreased HMF-to-BHMF conversion can be found after the t-BuOH was introduced into the system, because the H* were partly consumed by the t-BuOH rather than react with HMF. This indicates the H* generated through the Volmer step plays an essential role for the electrochemical hydrogenation of HMF.[37] To further explore the reaction mechanism, we investigated the dependence of the reaction rate on HMF concentration. According to the work by Lopez-Ruiz,[43] the reduction of HMF via the ECH process, HMF hydrogenation subsequent to H* formation—follows the Langmuir-Hinshelwood (L-H) mechanism, which is indicative of competitive adsorption between HMF and H_2O. Consequently, a negative reaction order with respect to HMF is anticipated at higher concentrations. As depicted in **Figure S10**, a negative reaction order was observed over the catalyst with increasing HMF concentration. This observation, consistent with the t-BuOH H* species scavenging experiment, collectively confirms that the reaction indeed adheres to the Langmuir-Hinshelwood (L-H) mechanism. Then, the reaction energetics were modeled under operando neutral conditions (0.5 M $KHCO_3$, pH=8.17), where the L-H mechanism dominates through surface-adsorbed hydrogen (H*) intermediates.[44]

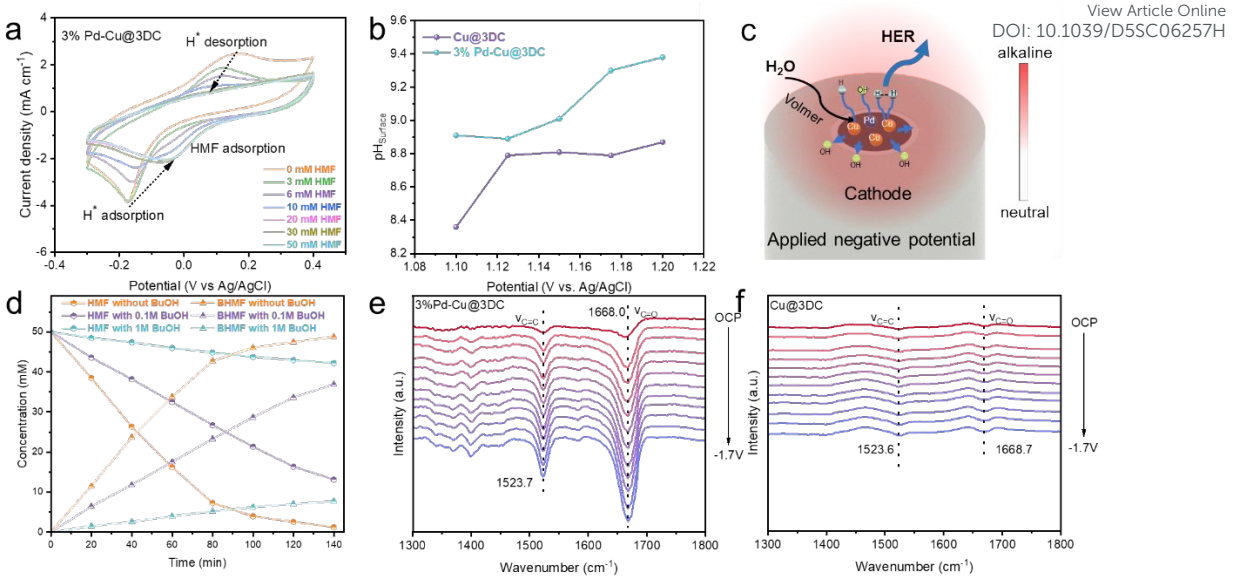

Figure 4. Electrocatalytic reaction mechanism analysis. (a) CV curves of 3%Pd-Cu@3DC in 0.5 M $KHCO_3$ with different HMF concentrations. (b) Local pH values on the surface of 3%Pd-Cu@3DC and Cu@3DC at varied potentials. (c) Schematic illustration of the OH^- enrichment effect on the 3%Pd-Cu@3DC for electrochemical HMF hydrogenation. (d) t-BuOH scavenges the H* species experiments. (e-f) In situ ATR-SEIRAS spectroscopy recorded on (e) 3%Pd-Cu@3DC and (f) Cu@3DC.

Density functional theory (DFT) calculations were systematically performed to elucidate the atomic-scale mechanism governing HMF hydrogenation and competing hydrogen evolution reaction (HER) pathways on Pd-Cu@3DC. Surface slab models of Cu(111) and Pd-doped Cu(111) were constructed based on the experimental results, and the Gibbs free energies of H* (ΔG_{H^*}) and HMF* adsorptions (ΔG_{HMF^*}) are also calculated. The pristine Cu(111) surface exhibits a ΔG_{H^*} value of -3.53 eV on the Cu sites, which suggests weak affinity for the H* atom. Interestingly, the Cu site near the Pd atom of the Pd-Cu exhibits a relatively lower ΔG_{H^*} of -3.58 eV, demonstrating the crucial role of Pd doping to afford Cu active site for H* adsorption (**Figure 5a**). It is

View Article Online
DOI: 10.1039/D5SC06257H

noteworthy that the catalyst must facilitate the activation and dissociation of H_2O to produce adsorbed H* species on its surface during the L-H mechanism. Therefore, we also assess the free energy change during the formation of OH^- and H* from H_2O. As shown in **Figure 5b**, the calculated energy barrier for each step of H_2O conversion to OH^- and H* on Pd-Cu model (1.23 eV) is lower than that on Cu model (1.54 eV).

Generally, the changes of open circuit potential (OCP) reflect the HMF adsorption ability on the catalyst surface.[45] As depicted in **Figure 5c**, as the Pd doping content increases, the magnitude of the OCP elevation following the introduction of 50 mM HMF also increases. For Pd@3DC, the OCP increases by 0.1338V after HMF introduction, which is approximately five times that of Cu@3DC (0.0266V), demonstrating that Pd exhibits a specific affinity for HMF adsorption. In addition, the calculated ΔG_{HMF*}(**Figure 5d**) results suggest that HMF prefers to adsorb on the Pd site with ΔG_{HMF*} of –0.85 eV, while it is weakly adsorbed on Cu (–0.68 eV). The longer C=O bond length (1.25 Å) of HMF molecules on the surface of Pd-Cu than on the Cu (1.24 Å) also indicates that Pd-Cu possesses stronger activation effect toward HMF. The potential-dependent in situ ATR-SEIRAS of 3% Pd-Cu@3DC (**Figure 4e-f**) exhibits an intensified C=O stretching band at 1668 cm^{-1} and a stronger C=C stretching band at 1523 cm^{-1} compared to Cu@3DC, which demonstrates the strong adsorption of HMF on the catalyst surface.[46] **Figure 5e** shows the optimized free energies of hydrogenation pathway from HMF to BHMF on both model surfaces. It is evident that the hydrogenation of HMF requires an energy uphill process with ΔG of 0.79 eV for the Pd-Cu, which is smaller than that of Cu (0.90 eV). The results imply that HMF

View Article Online
DOI: 10.1039/D5SC06257H

hydrogenation could be energetically more favored on Pd-Cu, further revealing the crucial role of Pd doping. Pd exhibits a much stronger adsorption affinity for HMF than Cu. However, poor product desorption may compromise its HMF hydrogenation efficiency (**Figure S4c**). In contrast, pure Cu exhibits inferior water dissociation capability, failing to generate sufficient H* species and thus rendering HMF hydrogenation inefficient ((**Figure S4a**). Thus, we propose that in the present system, Pd sites generate H* via the Volmer step, while synergizing with Cu to adsorb HMF molecules, thereby accelerating the hydrogenation process.

Therefore, a reaction mechanism is proposed herein **(Figure 5f**). Initially, a H_2O molecule is acquired to adsorb on the electrode. Under the role of the electrons and the active sites, H_2O was spitted to generate H*. Meanwhile, HMF is adsorbed on the Pd site to form HMF*, and the -CH=O was activated. Subsequently, HMF hydrogenation process proceeds via initial hydrogenation on C site and followed on O site in the aldehyde group.[44, 47] Additionally, HER is discerned as the main competing reactions in this process, due to the coupling of H* to form H_2. Consequently, it is crucial to optimize the reaction conditions and achieve a balance between the HMF hydrogenation reaction and the HER by adjusting parameters such as the HMF concentration, electrolytic potential, and even the catalyst materials.

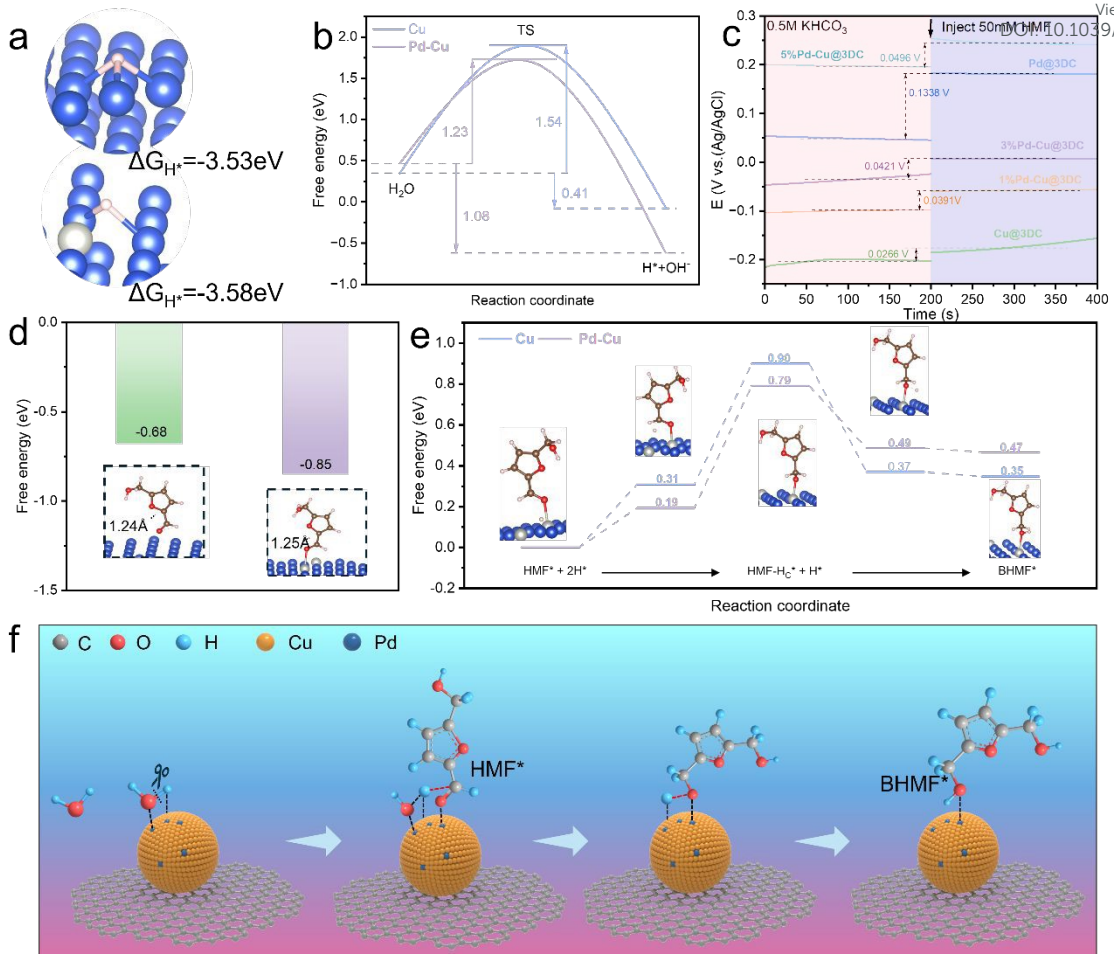

Figure 5. DFT theoretical calculations for the reaction pathway and mechanism on Pd-Cu and Cu for HMF hydrogenation to BHMF. (a) Adsorption free energy (ΔG_{H^*}) of H* and (b) the calculated ΔG for water splitting to produce an adsorbed H* species on Pd-Cu and Cu. (c) OCP curves of Cu@3DC, 1%Pd- Cu@3DC, 3%Pd-Cu@3DC, 5%Pd-Cu@3DC and Pd@3DC in 0.5M $KHCO_3$ solution and 0.5M $KHCO_3$ + 50 mm HMF solution. (d) Adsorption free energy (ΔG_{HMF^*}) of HMF and (e) the calculated ΔG for HMF hydrogenation to BHMF on Pd-Cu and Cu. (f) Proposed mechanism of HMF electrochemical reduction on 3%Pd-Cu@3DC.

View Article Online
DOI: 10.1039/D5SC06257H

BHMF Production and Application

Considering the superior performance of the 3%Pd-Cu@3DC, we further explored its successive production capability for the HMF electrochemical hydrogenation by applying proton exchange membrane (PEM) based flow reactor. As shown in **Figure S14**, a photograph of the PEM flow reactor for the continuous electroreduction of HMF to BHMF is presented. HMF solution is fed into the cathodic chamber, transported to the catalyst surface and electrochemically reduced to the targeted BHMF (**Figure 6a**). As shown in **Figure 6b**, the conversion and FE increase with the applied potential elevated from -1.6 to -2.4V. When the potential was elevated to -2.4V, a maximum BHMF conversion of 91%, with a current of -60 mA and FE of 99%. Once the potential continues to increase, FE will decrease due to the competition of HER. The stability was also preliminarily evaluated at -2.4V, maintaining an FE of above 95% and a conversion of 90% in 12 h electrolysis (**Figure 6c**). The BHMF was obtained from the effluent by evaporation crystallization - extraction - evaporation crystallization strategy (**Figure S8**). As shown in **Figure S8**, the obtained product is similar to the BHMF purchased from Aladdin, with a purity of 99%.

Next, to assess the techno-economic viability of the successive production for electrocatalysis HMF into BHMF, we proposed an integrated process model, encompassing the electrolyzer, evaporation crystallization, and extraction (**Figure 6d**). The model aligned operating parameters with experimental results from the PEM electrolyzer. The system produces 1 ton (t) day^{-1} of BHMF using 1.16 t day^{-1} HMF. As

View Article Online
DOI: 10.1039/D5SC06257H

shown in subdivided cost evaluation (**Figure 6e**), BHMF can be produced at the cost of \$626.4 t^{-1} via the cascade process. Among the cost, separation equipment account for 17.5%, followed by electrolyzer (16.7%) and catalyst-membrane cost (16.5%). In addition, economic analysis showed a 20-year net present value (NPV) of \$40 million and a 2-year payout period **(Figure 6f**). These results reveal that using renewable energy electrocatalytic HMF hydrogenation to prepare BHMF possesses high economic feasibility.

Finally, we demonstrated the downstream application of BHMF as a versatile building block for producing bio-based polyester. Poly(2,5-furandimethylene succinate) (PFS) was synthesized by solution condensation polymerization between BHMF and succinic acid (**Figure 6g**). GPC results confirmed that the molecular weight (M_n) of the obtained PFS was ~10861 and the polydispersity was 1.78 (**Figure S9a**, **Table S1**). Additionally, DSC analysis illustrates that the obtained PFS exhibits a Tg (glass transition temperature) of 50.6˚C and a Tm (melting onset temperature) of 85.2 ˚C (**Figure S9b**). These characters illustrate the high potential of the renewable PFS to play a role in a sustainable and circular plastic market.

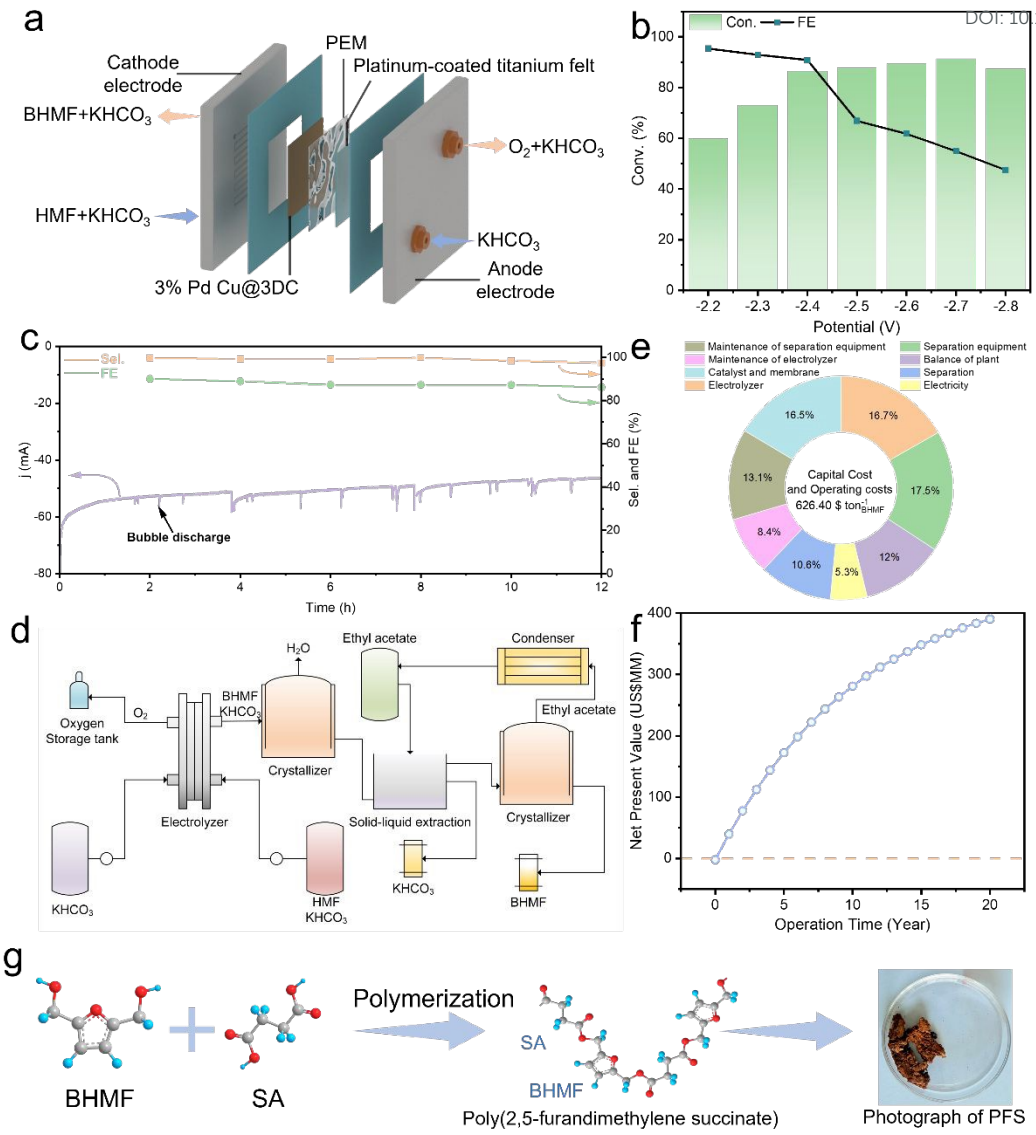

Figure 6. (a) Schematic illustration of a PEM electrolyzer. (b) HMF conversion at different potential. (c) Selectivity and FE of BHMF during chronoamperometry test. (d) Integrated process model for BHMF production. (e) Proportion of expenses in each part of the production process. (f) NPV curve in 20 years. (g) BHMF polymerize with SA to produce PFS.

Conclusion

In summary, novel Pd-Cu@3DC catalysts were constructed by a salt template

View Article Online
DOI: 10.1039/D5SC06257H

space-confined strategy. The unique atomic-level doping with internal charge transfer provides sites for enhanced adsorption and activation of H_2O molecules to facilitate H* generation. Interestingly, the obtained Pd-Cu@3DC exhibits high BHMF selectivity and FE yield of 99.3 % and 97.5 %, respectively, at –1.15 V (vs. Ag/AgCl), and maintains 13 cycles without obvious decay. Mechanism study reveals that Pd doping enhances the adsorption of H* and HMF*, promotes the hydrogenation steps by lowering the energy barrier of crucial step. These results described a novel method for further applications while providing an in-depth understanding of doping engineering in electrocatalysts to regulate electrocatalytic activity and selectivity.

Author contributions

Conflicts of interest

There are no conflicts to declare.

Data availability

All the data supporting this article has been included in the main text and the ESI.

Acknowledgements

This work was supported by the National Natural Science Foundation of China, China (grant numbers 52101263), the Shandong Provincial Natural Science Foundation, China (grant numbers ZR2021QE231, ZR2020QB048).

Author contributions:

G. F.: investigation, data collection; Y. F.: software, validation; L. D.: methodology, writing – review & editing, funding acquisition; Z. M.: funding acquisition; J. Z.: supervision.

Notes and references

(1) Hu, B.; Lu, Q.; Jiang, X.; Dong, X.; Cui, M.; Dong, C.; Yang, Y. Pyrolysis

mechanism of glucose and mannose: The formation of 5-hydroxymethyl furfural and furfural. *Journal of Energy Chemistry* **2018**, *27* (2), 486–501. DOI: 10.1016/j.jechem.2017.11.013.

(2) Li, Z.; Sun, J.; Wang, Y.; Song, Y.; Yang, J.; Liu, X.; Zhang, L. Construction of CoO–Cu_2O Composites With Enhanced HMF Adsorption and Passivated Water Oxidation for High-Efficiency Biomass Valorization. *ACS Sustainable Chemistry & Engineering* **2025**, *13* (15), 5645–5654. DOI: 10.1021/acssuschemeng.5c00177.

(3) Hou, Q.; Qi, X.; Zhen, M.; Qian, H.; Nie, Y.; Bai, C.; Zhang, S.; Bai, X.; Ju, M. Biorefinery Roadmap Based on Catalytic Production and Upgrading 5-Hydroxymethylfurfural. *Green Chemistry* **2021**, *23* (1), 119–231. DOI: 10.1039/d0gc02770g.

(4) Zhu, P.; Shi, M.; Shen, Z.; Liao, X.; Chen, Y. Electrocatalytic Conversion of Biomass-Derived Furan Compounds: Mechanisms, Catalysts and Perspectives. *Chemical Science* **2024**, *15* (13), 4723–4756. DOI: 10.1039/d4sc00546e.

(5) Xu, C.; Paone, E.; Rodríguez-Padrón, D.; Luque, R.; Mauriello, F. Recent catalytic routes for the preparation and the upgrading of biomass derived furfural and 5-hydroxymethylfurfural. *Chemical Society Reviews* **2020**, *49* (13), 4273–4306. DOI: 10.1039/d0cs00041h.

(6) Wang, G.-H.; Hilgert, J.; Richter, F. H.; Wang, F.; Bongard, H.-J.; Spliethoff, B.; Weidenthaler, C.; Schüth, F. Platinum–cobalt bimetallic nanoparticles in hollow carbon nanospheres for hydrogenolysis of 5-hydroxymethylfurfural. *Nature Materials* **2014**, *13* (3), 293–300. DOI: 10.1038/nmat3872.

(7) Wang, S.; Song, G. A pathway to bio-based aromatics. *Nature Sustainability* **2023**, *6* (11), 1295–1296. DOI: 10.1038/s41893-023-01191-9.

(8) Zhang, J.; Qin, H.; Cao, X.; Jia, W.; Ma, R.; Chen, X.; Xia, W.; Lin, G.; Jiao, L. Constructing Adjustable Heterointerface for Enhancing Acidic Oxygen Evolution Performances of RuO_2@$CoMnO_3$ Nanosheets Electrocatalysts. *ACS Materials Letters* **2024**, *6* (7), 3016–3024. DOI: 10.1021/acsmaterialslett.4c00778.

(9) Guo, Y. F.; Yang, L.; Zhang, L. Z.; Chen, S.; Sun, L. J.; Gu, S. J.; You, Z. W. A Dynamically Hybrid Crosslinked Elastomer for Room-Temperature Recyclable

Flexible Electronic Devices. *Advanced Functional Materials* **2021**, *31* (50). DOI: 10.1002/adfm.202106281.

(10) Ratrey, G.; Solanki, B. S.; Kamble, S. P.; Rode, C. V. Highly Efficient Chemoselective Hydrogenation of 5-HMF to BHMF over Reusable Bimetallic Pd-Ir/C Catalyst. *ChemistrySelect* **2022**, *7* (23). DOI: 10.1002/slct.202200456.

(11) Kang, B.; Chen, Z.; Yang, J.; Lv, M.; He, H.; Chen, G.; Huai, L.; Chen, C.; Zhang, J. Boosting Hydrogenation Properties of Supported Cu-Based Catalysts by Replacing Cu_0 Active Sites. *Applied Catalysis B: Environment and Energy* **2025**, *361*. DOI: 10.1016/j.apcatb.2024.124563.

(12) Kwon, Y.; Schouten, K. J. P.; van der Waal, J. C.; de Jong, E.; Koper, M. T. M. Electrocatalytic Conversion of Furanic Compounds. *ACS Catalysis* **2016**, *6* (10), 6704–6717. DOI: 10.1021/acscatal.6b01861.

(13) Linghu, X.; Chen, J.; Jiang, L.; Wang, T. Recent progress in bismuth-based materials for electrochemical CO_2 reduction to formate/formic acid. *Nano Materials Science* **2024**. DOI: 10.1016/j.nanoms.2024.11.007.

(14) Ali, T.; Wang, H.; Iqbal, W.; Bashir, T.; Shah, R.; Hu, Y. Electro-Synthesis of Organic Compounds with Heterogeneous Catalysis. *Advanced Science* **2022**, *10* (1) : 2205077. DOI: 10.1002/advs.202205077.

(15) Yap, F. M.; Sheng Ling, G. Z.; Su, B. J.; Loh, J. Y.; Ong, W.-J. Recent advances in structural modification on graphitic carbon nitride ($g\text{-}C_3N_4$)-based photocatalysts for high-efficiency photocatalytic H_2O_2 production. *Nano Research Energy* **2024**, *3*(1): 1-51 DOI: 10.26599/nre.2023.9120091.

(16) Chadderdon, X. H.; Chadderdon, D. J.; Matthiesen, J. E.; Qiu, Y.; Carraher, J. M.; Tessonnier, J. P.; Li, W. Mechanisms of Furfural Reduction on Metal Electrodes: Distinguishing Pathways for Selective Hydrogenation of Bioderived Oxygenates. *Journal of American Chemical Society* **2017**, *139* (40), 14120–14128. DOI: 10.1021/jacs.7b06331.

(17) Zhu, B.; Yang, J.; Wang, Q.; Yu, X.; Fan, S.; Xie, W.; Zhang, J.; Chen, C. Corrosion-Induced CoCu Microwire Arrays for Efficient Electroreduction of 5-Hydroxymethylfurfural. *Chem Catalysis* **2025**, *5* (4):101259. DOI:

View Article Online
DOI: 10.1039/D5SC06257H

10.1016/j.checat.2024.101259.

(18) Zhang, Y.-R.; Wang, B.-X.; Qin, L.; Li, Q.; Fan, Y.-M. A non-noble bimetallic alloy in the highly selective electrochemical synthesis of the biofuel 2,5-dimethylfuran from 5-hydroxymethylfurfural. *Green Chemistry* **2019**, *21* (5), 1108–1113. DOI: 10.1039/c8gc03689f.

(19) Ciotti, A.; Rahaman, M.; Yeung, C. W. S.; Li, T.; Reisner, E.; García-Melchor, M. Driving Electrochemical Organic Hydrogenations on Metal Catalysts by Tailoring Hydrogen Surface Coverages. *Journal of the American Chemical Society* **2025**, *147* (16), 13158–13168. DOI: 10.1021/jacs.4c15821.

(20) Li, S.; Kan, Z.; Bai, J.; Ma, A.; Lu, J.; Liu, S. Rational Design of Transition-Metal-Based Catalysts for the Electrochemical 5-Hydroxymethylfurfural Reduction Reaction. *ChemSusChem* **2024**, *17* (24): e202400869. DOI: 10.1002/cssc.202400869.

(21) Tian, C.; Yu, J. Q.; Zhou, D. J.; Ze, H. J.; Liu, H. Z.; Chen, Y. J.; Xia, R.; Ou, P. F.; Ni, W. Y.; Xie, K.; et al. Reduction of 5-Hydroxymethylfurfural to 2,5-Bis(hydroxymethyl)Furan at High Current Density using a Ga-Doped AgCu:Cationomer Hybrid Electrocatalyst. *Advanced Materials* **2024**, *36* (24): 2312778. DOI: 10.1002/adma.202312778.

(22) Cao, X.; Ding, Y.; Chen, D.; Ye, W.; Yang, W.; Sun, L. Cluster-Level Heterostructure of PMo12/Cu for Efficient and Selective Electrocatalytic Hydrogenation of High-Concentration 5-Hydroxymethylfurfural. *Journal of the American Chemical Society* **2024**, *146* (36), 25125–25136. DOI: 10.1021/jacs.4c08205.

(23) Zhang, W.; Ge, W.; Qi, Y.; Sheng, X.; Jiang, H.; Li, C. Surfactant Directionally Assembled at the Electrode-Electrolyte Interface for Facilitating Electrocatalytic Aldehyde Hydrogenation. *Angewandte Chemie International Edition* **2024**, *63* (31): e202407121. DOI: 10.1002/anie.202407121.

(24) Hauke, P.; Merzdorf, T.; Klingenhof, M.; Strasser, P. Hydrogenation Versus Hydrogenolysis during Alkaline Electrochemical Valorization of 5-Hydroxymethylfurfural Over Oxide-Derived Cu-Bimetallics. *Nature Communications* **2023**, *14* (1): 4708. DOI: 10.1038/s41467-023-40463-y.

(25) Zhao, Z.; Yu, R.; Wang, S.; Guo, L.; Zhang, L.; Chen, M.; Chen, J.; Zheng, H. Introducing Fe into Cu-Based Catalyst to Boost The Electrocatalytic Hydrogenation of 5-Hydroxymethylfurfural. *ChemSusChem* **2025,** *18*(1): e202401278. DOI: 10.1002/cssc.202401278.

(26) Guo, R.; Zeng, Y.; Lin, L.; Hu, D.; Lu, C.; Conroy, S.; Zhang, S.; Zeng, C.; Luo, H.; Jiang, Z.; et al. CO_2-Assisted Controllable Synthesis of PdNi Nanoalloys for Highly Selective Hydrogenation of Biomass-Derived 5-Hydroxymethylfurfural. *Angewandte Chemie International Edition* **2024**, *64* (6): e202418234. DOI: 10.1002/anie.202418234.

(27) Boro, B.; Koley, P.; Boruah, A.; Hosseinnejad, T.; Lee, J. M.; Chang, C.-C.; Pao, C.-W.; Bhargava, S.; Mondal, J. Deciphering Reactivity Factors of Cu(II)–Pd(0) Engaged in Porous Organic Polymer toward Catalytic Hydrogenolysis of 5-Hydroxymethylfurfural to 2,5-Dimethylfuran. *ACS Sustainable Chemistry & Engineering* **2024**, *12* (38), 14200–14217. DOI: 10.1021/acssuschemeng.4c04337.

(28) Cui, K.; Wang, T.; Zhang, Q.; Zhang, H. Multi-Functional Descriptor Design of V-Based Double Atomic Catalysts for Room Temperature Sodium-Sulfur Batteries. *Small* **2024**, *21* (4) 2409866. DOI: 10.1002/smll.202409866.

(29) Diao, L.; Zhang, B.; Sun, Q.; Wang, N.; Zhao, N.; Shi, C.; Liu, E.; He, C. An in-plane Co_9S_8@MoS_2 heterostructure for the hydrogen evolution reaction in alkaline media. *Nanoscale* **2019**, *11* (44), 21479–21486. DOI: 10.1039/c9nr06609h.

(30) Deng, Y.; Wang, J.; Zhang, S.-F.; Zhang, Z.-J.; Sun, J.-F.; Li, T.-T.; Kang, J.-L.; Liu, H.; Bai, S. In Situ Constructing Lamella-Heterostructured Nanoporous CoFe/$CoFe_2O_4$ and CeO_{2-x} as Bifunctional Electrocatalyst for High-Current-Density Water Splitting. *Rare Metals* **2024**, *44* (2), 1053–1066. DOI: 10.1007/s12598-024-02926-z.

(31) Li, L.; Wang, P.; Shao, Q.; Huang, X. Metallic nanostructures with low dimensionality for electrochemical water splitting. *Chemical Society Reviews* **2020**, *49* (10), 3072–3106. DOI: 10.1039/d0cs00013b.

(32) Jiang, W.; Liu, J. K.; Zhou, H.; Huang, Z. J.; Wu, Y. X.; Cao, S.; Yang, D. X.; Wang, X. L.; Liu, P. F.; Zhou, Y. Operando *OH Tracking Unveils Heteroatom-

Tailored Co_3O_4 Spinel Catalyst for Industrial-Level Current Density Ethylene Glycol Electrooxidation. *ACS Catalysis* **2025**, *15* (21), 18612–18622. DOI: 10.1021/acscatal.5c06358.

(33) Zheng, M.; Wang, P.; Gao, Y.; Peng, C.; Zheng, Y.; Qiao, S.-Z. Tuning interfacial *H coverage and aldehyde adsorption configuration for selective electrocatalytic hydrogenation of furfural. *Journal of Materials Chemistry A* **2025**, *13* (13), 9135–9143. DOI: 10.1039/d5ta00403a.

(34) Sendeku, M. G.; Harrath, K.; Dajan, F. T.; Wu, B.; Hussain, S.; Gao, N.; Zhan, X.; Yang, Y.; Wang, Z.; Chen, C.; et al. Deciphering In-situ Surface Reconstruction in Two-Dimensional CdPS3 Nanosheets for Efficient Biomass Hydrogenation. *Nature Communications* **2024**, *15* (1): 5174. DOI: 10.1038/s41467-024-49510-8.

(35) Peng, L.; Yu, Y.; Gao, S.; Wang, M.; Zhang, J.; Zhang, R.; Jia, W.; Sun, Y.; Liu, H. Coupling Cu+ Species and Zr Single Atoms for Synergetic Catalytic Transfer Hydrodeoxygenation of 5-Hydroxymethylfurfural. *ACS Catalysis* **2024**, *14* (9), 6623–6632. DOI: 10.1021/acscatal.4c00763.

(36) Zeradjanin, A. R.; Narangoda, P.; Masa, J.; Schlögl, R. What Controls Activity Trends of Electrocatalytic Hydrogen Evolution Reaction?─Activation Energy Versus Frequency Factor. *ACS Catalysis* **2022**, *12* (19), 11597–11605. DOI: 10.1021/acscatal.2c02964.

(37) Xu, H.; Xu, G.; Huang, B.; Yan, J.; Wang, M.; Chen, L.; Shi, J. Zn-Organic Batteries for the Semi-Hydrogenation of Biomass Aldehyde Derivatives and Concurrently Enhanced Power Output. *Angewandte Chemie International Edition* **2023**, *62* (20): e202218603. DOI: 10.1002/anie.202218603.

(38) Wen, H.; Fan, Z.; Dou, S.; Lam, J. C.-H.; Zhang, W.; Chen, Z. Electrochemical hydrogenation of furfural under alkaline conditions with enhanced furfuryl alcohol selectivity by self-grown Cu on a Ag electrode. *Inorganic Chemistry Frontiers* **2024**, *11* (14), 4449–4458. DOI: 10.1039/d4qi00763h.

(39) Ji, K.; Xu, M.; Xu, S. M.; Wang, Y.; Ge, R.; Hu, X.; Sun, X.; Duan, H. Electrocatalytic Hydrogenation of 5-Hydroxymethylfurfural Promoted by a Ru_1Cu Single-Atom Alloy Catalyst. *Angewandte Chemie International Edition* **2022**, *61* (37):

View Article Online
DOI: 10.1039/D5SC06257H

e202209849. DOI: 10.1002/anie.202209849.

(40) Zheng, X.; Shi, X.; Ning, H.; Yang, R.; Lu, B.; Luo, Q.; Mao, S.; Xi, L.; Wang, Y. Tailoring a Local Acid-like Microenvironment for Efficient Neutral Hydrogen Evolution. *Nature Communications* **2023**, *14* (1):4209. DOI: 10.1038/s41467-023-39963-8.

(41) Huang, B.; Yan, J.; Li, Z.; Chen, L.; Shi, J. Anode-Electrolyte Interfacial Acidity Regulation Enhances Electrocatalytic Performances of Alcohol Oxidations. *Angewandte Chemie International Edition* **2024**, 63(40): e202409419. DOI: 10.1002/anie.202409419.

(42) Tang, S.; Guo, N.; Chen, C.; Yao, B.; Liu, X.; Ma, C.; Liu, Q.; Ren, S.; He, C.; Liu, B.; et al. Electrochemical Alkyne Semi-Hydrogenation via Proton-Coupled Electron Transfer on Cu(111) Surface. *Angewandte Chemie International Edition* **2025**, 137(37): e202510192. DOI: 10.1002/anie.202510192.

(43) Lopez-Ruiz, J. A.; Sanyal, U.; Egbert, J.; Gutiérrez, O. Y.; Holladay, J. Kinetic Investigation of the Sustainable Electrocatalytic Hydrogenation of Benzaldehyde on Pd/C: Effect of Electrolyte Composition and Half-Cell Potentials. *ACS Sustainable Chemistry & Engineering* **2018**, *6* (12), 16073–16085. DOI: 10.1021/acssuschemeng.8b02637.

(44) Sendeku, M. G.; Harrath, K.; Dajan, F. T.; Wu, B.; Hussain, S.; Gao, N.; Zhan, X.; Yang, Y.; Wang, Z.; Chen, C.; et al. Deciphering in-situ surface reconstruction in two-dimensional CdPS3 nanosheets for efficient biomass hydrogenation. *Nature Communications* **2024**, *15* (1). 15:5174 DOI: 10.1038/s41467-024-49510-8.

(45) Chen, Y.; Qiu, J.; Li, S.; Zhang, J.; Liu, Y.; Chen, X.; Liu, X.; Dou, S.; Wang, D. Spontaneous Corrosion Induced Scalable Fabrication of Bayberry-Like Ni@Ni3S2 Core–Shell Catalysts for 5-Hydroxymethylfurfural Oxidation. *Advanced Functional Materials* **2024**, *35* (5): 2414587. DOI: 10.1002/adfm.202414587.

(46) Wu, Y.; Jiang, Y.; Chen, W.; Yue, X.; Dong, C. L.; Qiu, M.; Nga, T. T. T.; Yang, M.; Xia, Z.; Xie, C.; et al. Selective Electroreduction of 5-Hydroxymethylfurfural to Dimethylfuran in Neutral Electrolytes via Hydrogen Spillover and Adsorption Configuration Adjustment. *Advanced Materials* **2023**, *36* (7):2307799. DOI:

View Article Online
DOI: 10.1039/D5SC06257H

10.1002/adma.202307799.

(47) Guo, X.; Fu, H.; Yang, J.; Luo, L.; Zhou, H.; Xu, M.; Kong, X.; Shao, M.; Duan, H.; Li, Z. Promoting Electrocatalytic Hydrogenation of 5-Hydroxymethylfurfural over a Cooperative Ag/SnO_2 Catalyst in a Wide Potential Window. *ACS Catalysis* **2023**, *13* (20), 13528–13539. DOI: 10.1021/acscatal.3c03005.

View Article Online
DOI: 10.1039/D5SC06257H

All the data supporting this article have been included in the main text and the ESI.